Full atomistic reaction mechanism with kinetics for CO reduction on Cu(100) from ab initio molecular dynamics free-energy calculations at 298 K

Tao Cheng[a,b], Hai Xiao[a,b], and William A. Goddard III[a,b,1]

[a]Joint Center for Artificial Photosynthesis, California Institute of Technology, Pasadena, CA 91125; and [b]Materials and Process Simulation Center (MC139-74), California Institute of Technology, Pasadena, CA 91125

A critical step toward the rational design of new catalysts that achieve selective and efficient reduction of CO_2 to specific hydrocarbons and oxygenates is to determine the detailed reaction mechanism including kinetics and product selectivity as a function of pH and applied potential for known systems. To accomplish this, we apply ab initio molecular metadynamics simulations (AIMμD) for the water/Cu(100) system with five layers of the explicit solvent under a potential of −0.59 V [reversible hydrogen electrode (RHE)] at pH 7 and compare with experiment. From these free-energy calculations, we determined the kinetics and pathways for major products (ethylene and methane) and minor products (ethanol, glyoxal, glycolaldehyde, ethylene glycol, acetaldehyde, ethane, and methanol). For an applied potential (U) greater than −0.6 V (RHE) ethylene, the major product, is produced via the Eley–Rideal (ER) mechanism using $H_2O + e^-$. The rate-determining step (RDS) is C–C coupling of two CO, with $\Delta G^{\ddagger} = 0.69$ eV. For an applied potential less than −0.60 V (RHE), the rate of ethylene formation decreases, mainly due to the loss of CO surface sites, which are replaced by H*. The reappearance of C_2H_4 along with CH_4 at U less than −0.85 V arises from *CHO formation produced via an ER process of H* with non-adsorbed CO (a unique result). This *CHO is the common intermediate for the formation of both CH_4 and C_2H_4. These results suggest that, to obtain hydrocarbon products selectively and efficiency at pH 7, we need to increase the CO concentration by changing the solvent or alloying the surface.

reaction mechanism | electrocatalysis | copper | QM metadynamics | free-energy reaction barriers

To reduce the carbon footprint while converting renewable energy sources (such as the wind or solar) into stable chemical forms, we need to develop an economical process for the CO_2 reduction reaction (CO_2RR) to chemicals and fuels. Copper (Cu) is the only nonalloyed metal that can electrochemically catalyze the formation of significant amounts of hydrocarbons (1). However, Cu leads to an overpotential of almost 1 V for a reasonable current (5–10 mA·cm^{-2}) and faradaic efficiency (>69%) (2), and it leads to a fairly broad mixture of major and minor products, including hydrogen (H_2), ethylene (C_2H_4), and methane (CH_4) as major products plus small amounts of other C_2s and oxygenates (3). Although Cu remains far from ideal for CO_2 reduction, it provides a benchmark for determining and validating the mechanism underlying Cu's unique ability to catalyze hydrocarbon formation. This mechanism can then provide a basis for designing new catalysts that increase product selectivity and rates while simultaneously lowering overpotentials.

Some excellent reviews summarize previous research associated with CO_2RR on copper (4–6). Although many aspects of the mechanism remain unknown, CO is established as an important intermediate producing both C_2H_4 and methane CH_4 as major products. Indeed electroreduction of CO leads to similar product distributions and onset potentials as observed for CO_2RR (5–8). Online electrochemical mass spectrometry (OLEMS)

was used to identify the products formed from the electroreduction of various compounds that might be intermediates on the C_2H_4 and ethanol (C_2H_5OH) pathways (3, 9).

The formation of CH_4 from CO depends on pH in such a way that the rate-determining step (RDS) must involve the transfer of a proton and an electron (10, 11). Recent experiments and density functional theory (DFT) calculations suggested that the key intermediate in the formation of CH_4 are *CHO on Cu(100) (12) and Cu(211) (13) and *COH on Cu(111) (14). On the other hand, the formation of C_2H_4 from CO does not depend on pH. Therefore, a dimer of CO, whose formation does not involve the transfer of a hydrogen atom but does depend on potential, has been suggested as the key intermediate in the C–C coupling (15).

The selectivity toward C_1 and C_2 production also depends on the surface structure of the copper electrode. For example, the formation of CH_4 is favored on Cu(111), whereas formation of C_2H_4 is dominant on Cu(100) (10, 16), and C_2H_5OH is generated at Cu(110) and Cu(511) (17). Evidence also exists that Cu polycrystalline (PC) generates ample amounts of C_2H_4 (3, 6), indicating that Cu(100) is the dominant crystal facet of Cu PC. Indeed, operando electrochemical scanning tunneling microscopy showed that a Cu PC electrode held at a fixed negative potential undergoes stepwise surface reconstruction to establish the Cu(100) surface (18).

Fig. 1 shows the competition between C_2H_4 formation, hydrogen evolution (HER), and CH_4 formation as a function of applied potential (U) observed experimentally in CO reduction reactions (CORR) on Cu(100) at pH 7 (11). C_2H_4 formation starts at $U = -0.40$ V [reversible hydrogen electrode (RHE)] and increases to a maximum at −0.60 V with a high current that is hard to explain by the reduction of a surface-adsorbed species (10).

Significance

Converting CO_2 to fuels is of great interest nowadays. Copper (Cu) is the only metal that produces hydrocarbon products, making it of interest for learning the reaction mechanisms underlying the selectivity and activity of Cu catalysts. In this report, we examine the reaction mechanism of CO reduction on Cu(100) at pH 7 including explicitly the aqueous solvent with ab initio molecular metadynamics simulations (AIMμD) free-energy calculations, which we find to explain all experimental observations. We expect that this understanding will suggest how to modify the Cu catalyst or replace it with a new material to enhance production of just a single such product while reducing the energy requirements (overpotential).
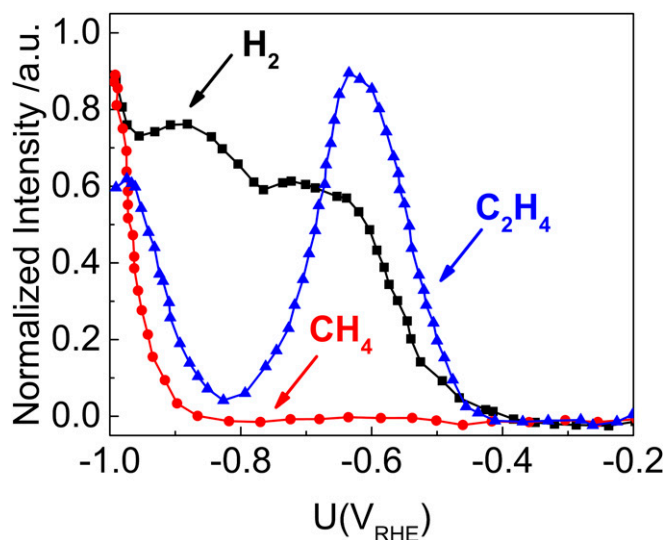
CHEMISTRY

Fig. 1. Experimental mass fragments of C_2H_4, H_2, and CH_4, determined with OLEMS for reduction of CO in 0.1 M phosphate buffers (pH 7). C_2H_4 products in blue triangles. H_2 products in black squares and CH_4 products in red circles. This figure is based on the experimental data from Schouten et al. (11).

Significant H_2 initiates at $U = -0.4$ V (RHE) and increases monotonically as U becomes more negative, which is the major contribution to current (10, 11). C_2H_4 formation decreases from −0.60 V (RHE) down to 0 at $U = -0.80$ V (RHE), whereas H_2 production increases but without producing CH_4. At $U = -0.85$ V (RHE), the formation of CH_4 first appears with C_2H_4 again observed, with both amounts increasing monotonically for more negative potentials.

Quantum-mechanical (QM) calculations can provide atomistic mechanistic insight about CORR (12–15, 19–22). However, previous studies have all been deficient in not fully including solvent effects. Early calculations ignored the solvent in the simulation but corrected afterward (13, 15), whereas later studies used a variety of implicit solvation methods sometimes with a few explicit solvent molecules (14). These various studies led to a range of inconsistent results. For example, the predicted free-energy barriers for CO dimerization range from 0.33 to 1.22 eV, depending on the solvation model (15, 20–22). Consequently, we concluded that it is essential to use multiple layers of explicit water to describe reactions at the catalyst–solvent interface properly.

In this paper, free energies were calculated by metadynamics (23, 24) and further converged using thermodynamic integration by constrained molecular dynamics (blue moon ensemble) (25) to explain the experimentally observed product distribution as a function of U for Cu(100). These free-energy calculations provide a thorough reaction mechanism for major hydrocarbon productions (ethylene and ethane) and minor productions in CORR, which should help guide the design of new generations of catalysts.

Results and Discussion

Applied Potentials Less Negative Than −0.6 V (U greater than −0.6 V). **C_2H_4 is the product with the lowest kinetic barrier.** For $U = -0.4$ to −0.6 V (RHE), our calculations with explicit solvent find that the most favorable reduction of CO is C–C coupling to form *CO–CO, which has a free-energy barrier for the transition state saddle point ($\Delta G^{\ddagger}$) of 0.69 eV. We find that *CO–CO is quickly hydrated to *CO–COH, which then is quickly reduced to *COH–COH. The reaction barriers for these two steps are both within 0.14 eV. Indeed, we observe these reactions directly in our ab initio molecular dynamics (AIMD) simulation, because the low

reaction barriers are surmounted within a few picoseconds. These reactions are via the Eley–Rideal (ER) mechanism using $H_2O + e^-$. Actually, in our calculations, we found that when adding hydrogen to oxygen, reactions via ER always have lower kinetic barriers than those via Langmuir–Hinshelwood (LH) mechanisms. The formation of *COH–COH explains the experimental observation of C_2 oxygenated products containing two oxygens, such as glycolaldehyde (CH_2OH–CHO) and ethylene glycol (CH_2OH–CH_2OH) (3).

Dihydroxylation of *COH–COH leads to the formation of *C–COH with $\Delta G^{\ddagger} = 0.62$ eV via ER. Reduction of *C–COH to *CH–COH has $\Delta G^{\ddagger} = 0.44$ eV via ER (0.91 eV via LH). The next step is dihydroxylation of *CH–COH to *CH–C with $\Delta G^{\ddagger} = 0.61$ eV via ER by using $H_2O + e^-$.

The reactions from *CH–C to C_2H_4 seem straightforward, showing selectivity toward hydrocarbon species. Thus, *CH–C is reduced to *CH$_2$–C instead of *CH–CH, because $\Delta G^{\ddagger} = 0.61$ eV (ER) for *CH$_2$–C formation ($\Delta G^{\ddagger} = 0.93$ eV via LH) is lower than the $\Delta G^{\ddagger} = 1.07$ eV (ER) for *CH–CH formation (1.41 eV via LH). We find that *CH$_2$–C is reduced to *CH$_2$–CH with $\Delta G^{\ddagger} = 0.49$ eV (ER) (1.10 eV via LH). Finally, formation of C_2H_4 from *CH$_2$–CH has $\Delta G^{\ddagger} = 0.38$ eV (ER) (1.15 eV via LH).

Summarizing, we find that adding hydrogen to carbon species through the ER mechanisms always has a lower reaction barrier than reactions through LH (Fig. 2) in the C_2H_4 formation pathway. Therefore, at $U = -0.59$ V (RHE) and pH 7, the lowest kinetic reaction pathway for C_2H_4 formation is purely through the ER mechanism, so that no step requires surface hydrogen (H*). This ER pathway explains the high current for C_2H_4 formation observed experimentally, which is beyond that expected from surface reactions (10). In this ER pathway of C_2H_4 formation, CO dimerization is the RDS with $\Delta G^{\ddagger} = 0.69$ eV.

The second pathway to the C_2H_4 product. A second pathway for C_2H_4 formation is through *CCO, which was first proposed by Calle-Vallejo and Koper (15). Indeed, *CCO formation is energetically more favorable on Cu(100), but $\Delta G^{\ddagger}$ for *CCO formation (0.69) is 0.67 eV higher than that of *COH–COH formation (0.02), making it kinetically forbidden. Thus, the *CCO pathway provides only a minor contribution to the C_2H_4 formation.

In this *CCO pathway for C_2H_4 formation, *CCO is first reduced to *CH–CO via LH with $\Delta G^{\ddagger} = 0.69$ eV. Then, *CH–CO is reduced to *CH–COH with $\Delta G^{\ddagger} = 1.49$ eV via LH, which merges into the *COH–COH pathway to also form C_2H_4.
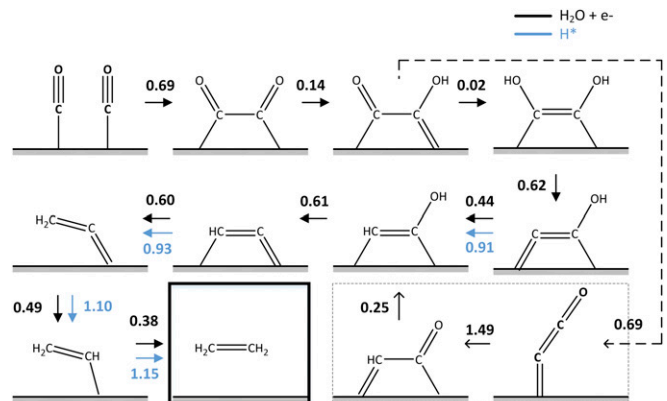
Fig. 2. Lowest kinetic pathways for the eight-electron reduction of CO to ethylene (C_2H_4). Both Eley–Rideal (ER) (in black) and Langmuir–Hinshelwood (LH) mechanisms (in blue) are considered. In ER, $H_2O + e^-$ (producing OH$^-$) are the reactants, whereas in LH, H* is the reactant. The reaction free-energy barriers ($\Delta G^{\ddagger}$) are provided. The slashed line shows the minor pathway for C_2H_4 formation through *C=C=O.

The entire reaction pathway for C_2H_4 formation is shown in Fig. 2. Snapshots of reactive intermediates from AIMD simulations are shown in Fig. 3.

Most kinetic favorable pathway to CH_4 products. The lowest energy pathway for CH_4 formation at pH 7 is as follows:

i) Reduction of CO to *CHO with an energy barrier of 0.96 eV via LH (0.97 eV via ER),
ii) Quick reduction of *CHO to *CHOH with $\Delta G^{\ddagger} = 0.24$ eV via ER,
iii) Then dehydroxylation of *CHOH leads to *CH + OH$^-$ with $\Delta G^{\ddagger} = 0.59$ eV via ER.
iv) Next is *CH reduction to *CH$_2$ with $\Delta G^{\ddagger} = 0.40$ eV via ER (0.97 eV via LH),
v) Then *CH$_2$ reduction to *CH$_3$ with $\Delta G^{\ddagger} = 0.55$ eV via ER (1.05 eV via LH),
vi) And finally, *CH$_3$ reduction to CH$_4$ with $\Delta G^{\ddagger} = 0.81$ eV via ER (0.86 eV via LH).

The entire reaction pathway for CH_4 formation is shown in Fig. 4. Snapshots of reactive intermediates from AIMD simulations are shown in Fig. 5.

At pH 7, *CHO formation is the RDS for CH_4 formation with $\Delta G^{\ddagger} = 0.96$ eV via LH, whereas CO dimerization is the RDS for C_2H_4 formation with $\Delta G^{\ddagger} = 0.69$ eV. Therefore, at pH 7, C_2H_4 is predominant for U greater than -0.8 V (RHE), as experimentally observed. Note that *CHO formation is pH dependent, whereas C–C coupling is pH independent (20). Thus, at pH 0, $\Delta G^{\ddagger}$ of *CHO formation decreases to 0.55 eV $(0.96 - 0.0592 \times 7)$, whereas the reaction barrier of C–C coupling remains at 0.69 eV. This pH dependency explains why CH_4 is predominant at pH 0, as experimentally observed (11).

HER is the major side reaction competing with CO reduction, which limits the faradaic efficiency. It is known that the presence of CO retards HER due to the stronger binding of CO to Cu metal surface (2). On the Cu(100) surface, our QM calculations with full solvation lead to a binding energy (ΔE_b) of -0.80 eV for CO and -0.11 eV for H atom (hollow site) reference to H_2. Therefore, at zero applied potential $(U = 0$ V$)$, the binding energy of CO is much larger than that of H*. The maximum CO coverage can reach 1/3 ML, as predicted in a previous DFT calculation (26).
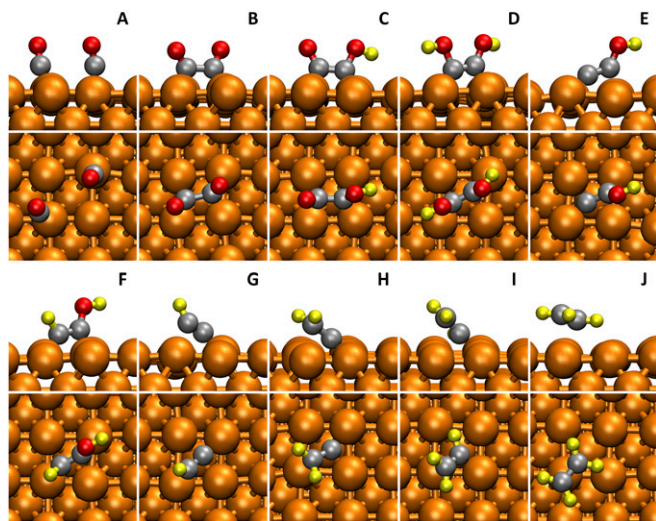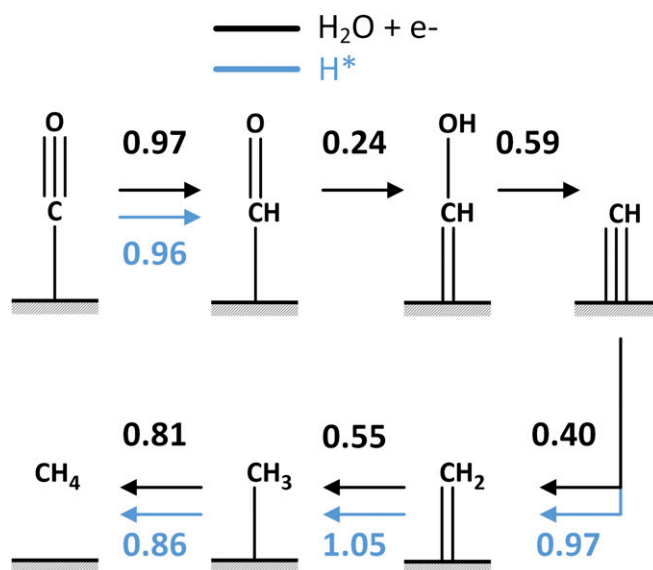

Fig. 4. Lowest kinetic pathway for the six-electron reduction of CO to methane (CH_4). Both the Eley–Rideal (ER) mechanism (in black) and the Langmuir–Hinshelwood (LH) mechanism (in blue) are considered. In the ER mechanism, $H_2O + e^-$ (producing OH$^-$) are the reactants, whereas in the LH mechanism, H* is the reactant. The reaction free-energy barriers ($\Delta G^{\ddagger}$) are provided.

Comparison with experiment and previous calculations. On the Cu(100) surface, C_2H_4 formation starts at $U = -0.4$ V and is pH independent (RHE dependent) (11), indicating that the RDS does not involve hydrogen. Additionally, no CH_4 formation is observed at this potential, pointing out that the mechanism is different from at U less than -0.8 V, where there is branching to both C_2H_4 and CH_4. These experimental observations agree with the theory that the first step of C_2H_4 formation is related to coupling of two CO molecules mediated by electron transfer to form *CO–CO.

We find that $\Delta G^{\ddagger} = 0.69$ eV for the RDS. Previous calculations of the reaction barrier for CO dimerization have ranged from 0.33 to 1.22 eV, depending on the solvation models and applied potentials (15, 20–22).

Potentials from -0.6 to -0.8 V. The above tendencies for U greater than -0.8 V are reversed for more negative U. As U becomes more negative, the ΔE_B of H increases with a slope close to 1 eV/V $[H_2O(aq) + e^- \rightarrow OH^-(aq) + H^*]$. In contrast, more negative U has little impact on ΔE_B of CO, because charges barely transfer during CO adsorption. To validate this, the charge transfers during CO adsorption were calculated under fixed applied potentials by optimizing the number of electrons (N_e) along the reaction path (27) within the framework of joint density functional theory (28), and the solvation effects was handled by the charge-asymmetric nonlocally determined local-electric implicit model (29). We find that, for increasingly negative U, ΔE_B of H* increases, and finally matches the CO binding at $U = -0.69$ V (RHE). Consequently, at U more negative than -0.69, surface H* and *CO compete for surface sites. Although no experimental data are available about the surface coverage of H under CORR condition, previous experimental studies (analyzed based on Volmer–Heyrovsky pathways and Volmer–Tafel pathways) estimated the surface coverage of H* to range from 0.3 to 1.0 at large negative overpotentials (30, 31).

Furthermore, experiments on Cu(100) starting from $U = -0.64$ to -0.70 V (saturated calomel electrode) or -0.40 to -0.46 V (RHE) suggest that H* induces reconstruction leading to a concomitant increase in HER (32). A recent in situ surface-enhanced spectroscopic experiment shows that at -0.7 V H* is

Fig. 3. Snapshots (side view and top view) of reactants (*A*), reactive intermediates (*B–I*), and production (*J*) in the ethylene (C_2H_4) pathway from AIMD simulations at 298 K. The solvent water molecules are hidden for viewing convenience. The colors are Cu in orange, C in gray, H in yellow, and O in red.
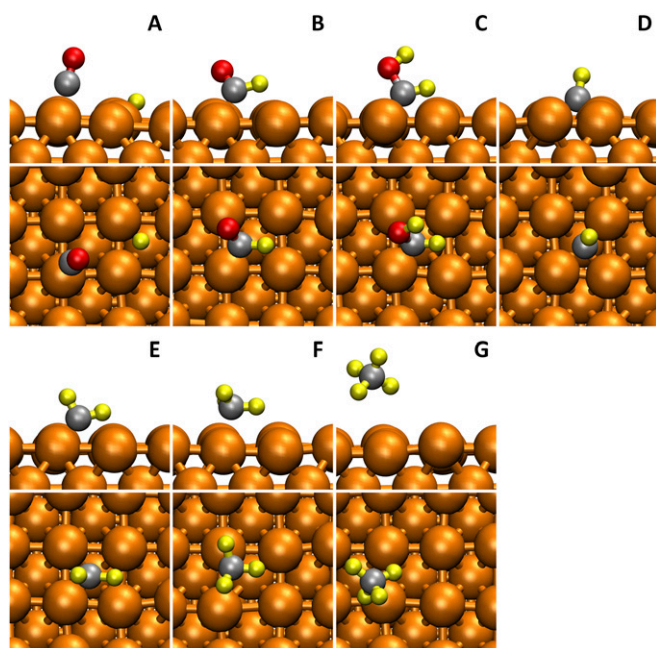
Fig. 5. Snapshots (side view and top view) of reactants (*A*), reactive intermediates (*B–F*), and production (*G*) in the methane (CH$_4$) pathway from AIMD simulations at 298 K. The solvent water molecules are hidden for viewing convenience. The colors are Cu in orange, C in gray, H in yellow, and O in red.

capable of partially displacing *CO; however, *CO is unable to displace H* to any detectable level (33). This increase in H* coverage causes a decrease in CO surface coverage that significantly slows the CO dimerization and hence C$_2$H$_4$ formation. We consider that site-blocking effects explain the decline of C$_2$H$_4$ formation down to 0 as $U = -0.60$ goes to -0.80 V (10, 11). Of course, we cannot exclude that other effects may contribute, such as deposition of metal impurities (34) and mass diffusion limitations (35).

Potentials are more negative than −0.8 V. Interestingly, we found that this site-blocking effect at very negative U does not block *CHO formation, which can be explained by *CHO formation proceeding via an ER mechanism from nonadsorbed CO. To demonstrate this, we carried out simulations for the extreme case of full H* (1 ML) coverage to block all available sites for CO adsorption. Under this condition, any CO on the surface would quickly desorb. With explicit solvent, we calculate that at 1-ML H* coverage, the distance of CO from the Cu surface is ~3.35 Å (as shown in Fig. 6*A*). We find that $\Delta G^{\ddagger} = 1.01$ eV for this solvent CO to react with a surface H* to produce *CHO, very close to the value ($\Delta G^{\ddagger} = 0.96$ eV) derived at low H* coverage for adsorbed CO to react with H*. As a consequence, the H* site-blocking effect does not block *CHO formation. Because *CHO formation can proceed from a reaction pathway in which CO is not adsorbed (as shown in Fig. 6), we can understand the appearance of CH$_4$ at U less than −0.85 V (RHE).

We calculate that recurrence of C$_2$H$_4$ for U less than −0.85 arises from the pathway in which nonadsorbed CO reacts with *CHO, as shown in Fig. 7. In this case, a second nonadsorbed CO reacts with *CHO to form *CO–CHO with $\Delta G^{\ddagger} = 0.71$ eV. Goodpaster et al. (21) first proposed this reaction pathway to explain the recurrence of C$_2$H$_4$ production. Although our predicted $\Delta G^{\ddagger}$ is close to the Goodpaster value, 0.68 eV, our reaction pathways are significantly different. Goodpaster assumed CO already adsorbed on the Cu surface based on his implicit solvation model, whereas we find that a nonadsorbed CO is a reactant in our explicit solvent calculations. Consequently,

our mechanism involves only one surface site (Fig. 7), which we expect to be close to the experimental conditions at U less than −0.85 V (RHE).

Summarizing, we find that the recurrence of C$_2$H$_4$ at U less than −0.85 V (RHE) is due to the coupling of nonadsorbed CO with *CHO. Consequently, C$_2$H$_4$ and CH$_4$ formation share a common intermediate, which explains the appearance of C$_2$H$_4$ and CH$_4$ following each other for $U < 0.85$ V (RHE).

Summary of Reaction Mechanism for CH$_4$ and C$_2$H$_4$ Products for All Potentials. Armed with the complete free-energy information from above, we can now explain the reaction mechanism of CORR on Cu(100) at pH 7 as follows:

- For U greater than −0.6 V (RHE), C$_2$H$_4$ is the major product through CO dimerization with $\Delta G^{\ddagger} = 0.69$ eV. We find that H$_2$O is the hydrogen source for all these reduction steps in C$_2$H$_4$ formation, leading to a high current as experimentally observed. CH$_4$ was not observed at U greater than −0.85 V (RHE), because *CHO formation is unfavorable due to the high reaction barrier ($\Delta G^{\ddagger} = 0.96$ eV via adsorbed CO and the $\Delta G^{\ddagger} = 1.01$ eV via nonadsorbed CO).
- As U decreases from −0.6 to −0.8 V, the H* binding energy increases, leading to an increased surface concentration of H*, with a concomitant decreased concentration of *CO, which significantly slows C$_2$H$_4$ formation and finally totally blocks this reaction for $U = -0.80$ V.
- At U less than −0.85 V, a nonadsorbed CO hydrogenation pathway contributes to the occurrence of CH4 in addition to the adsorbed CO pathway. The reoccurrence of C$_2$H$_4$ formation for U less than −0.85 V in parallel with CH$_4$ arises from *CO–CHO formation through nonadsorbed CO coupling with *CHO. Thus, *CHO is the common intermediate for both C$_2$H$_4$ and CH$_4$ formation at U less than −0.85 V.

Other Hydrocarbon and Oxygenate Products. Apart from the two major hydrocarbon products, small amounts of several other C1 to C3 products are observed experimentally under CO$_2$ reduction conditions (3). The mechanisms for the formation of these minor productions are also an important part of CORR and CO$_2$RR. We find the lowest kinetic reaction pathways to minor products of C$_2$ products at pH 7 proceed as follows (in each case, the number below the arrow is the $\Delta G^{\ddagger}$):
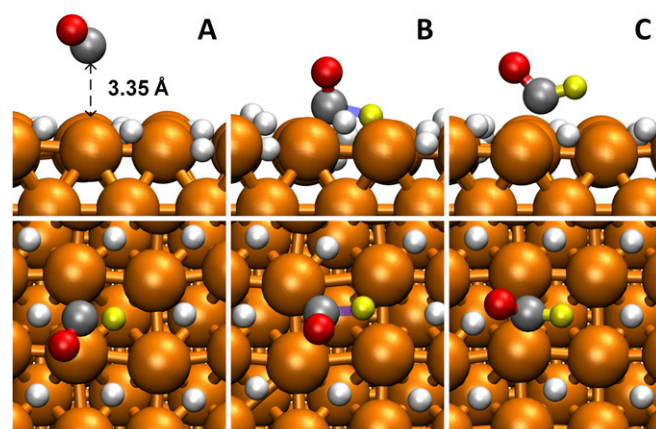

Fig. 6. Reactive trajectories of *CHO formation for high coverage of surface H (1 ML of H*) from AIMD simulations at 298 K (*A*) nonadsorbed CO, (*B*) transition state, and (*C*) *CHO. The solvent water molecules are hidden for viewing convenience. The colors are Cu in orange, C in gray, H in yellow, and O in red. The reaction barrier is 1.01 eV.

i) Glyoxal (CHO–CHO):

$$*\text{COH–COH} \xrightarrow[1.21]{} *\text{COH–CHO} \xrightarrow[1.22]{} \text{CHO–CHO}. \qquad [1]$$

ii) Glycolaldehyde (CHO–CH$_2$OH):

$$*\text{COH–COH} \xrightarrow[1.07]{H^*} *\text{CHOH–COH} \xrightarrow[1.13]{H^*}$$
$$\text{CHOH}=\text{CHOH} \xrightarrow[1.22]{H*} \text{CHO–CH}_2\text{OH}. \qquad [2]$$

iii) Ethylene glycol (CH$_2$OH–CH$_2$OH):

$$\text{CHOH}=\text{CHOH} \xrightarrow[1.51]{H^*} *\text{CH}_2\text{OH–CHOH}$$
$$\xrightarrow[0.83]{H^*} \text{CH}_2\text{OH–CH}_2\text{OH}. \qquad [3]$$

iv) Ethanol (CH$_3$–CH$_2$OH):

$$*\text{CH–COH} \xrightarrow[1.05]{H^*} *\text{CH–CHOH} \xrightarrow[1.14]{H^*} \text{CH}_2=\text{CHOH}$$
$$\xrightarrow[1.04]{H^*} \text{CH}_3\text{–CHOH} \xrightarrow[1.01]{H^*} \text{CH}_3\text{–CH}_2\text{OH}. \qquad [4]$$

v) Acetaldehyde (CH$_3$–CHO):

$$\text{CH}_2=\text{CHOH} \xrightarrow[1.22]{} \text{CH}_3\text{–CHO}. \qquad [5]$$

vi) Ethane (CH$_3$–CH$_3$):

$$*\text{CH}=\text{CH}_2 \xrightarrow[1.21]{H^*} *\text{CH–CH}_3 \xrightarrow[1.56]{H^*} \text{CH}_2\text{–CH}_3$$
$$\xrightarrow[1.24]{H^*} \text{CH}_3\text{–CH}_3. \qquad [6]$$

All these C products share the same reaction intermediate with C$_2$H$_4$: *COH–COH. They can be further partitioned into three groups based on how they branch from the C$_2$H$_4$ pathway:

i) Glyoxal (CHO–CHO) leaves the C$_2$H$_4$ pathway at *COH–COH by forming *COH–CHO through nonelectrochemical reaction steps, which are much slower than the *C–COH formation in the C$_2$H$_4$ pathway.

ii) Glycolaldehyde (CHO–CH$_2$OH) and ethylene glycol (CH$_2$OH–CH$_2$OH) leave the C$_2$H$_4$ pathway at *COH–COH by forming *CHOH–COH, which has a $\Delta G^\ddagger$ of 0.44 eV higher.

iii) C$_2$H$_5$OH, acetaldehyde (CH$_3$–CHO), and ethane (CH$_3$–CH$_3$) leave the C$_2$H$_4$ pathway at *CH–COH by forming *CH–COH, which has a $\Delta G^\ddagger$ of 0.43 eV higher. Of these three productions, C$_2$H$_5$OH formations are the fastest.

Experimentally, C$_2$H$_4$ and C$_2$H$_5$OH have similar Tafel slopes patterns, whereas CHO–CH$_2$OH has a different Tafel slope pattern (3). These observations provide experimental evidence showing that C$_2$H$_5$OH branches from the C$_2$H$_4$ pathway later than does CHO–CH$_2$OH, as predicted.

Conclusion

Summarizing, we carried out AIMD reactive dynamics simulations with five layers of explicit water to determine the mechanism of CORR on Cu(100) surface at pH 7. We determined the reaction pathways including free-energy reaction barriers for major products (C$_2$H$_4$ and CH$_4$), and for six minor C2 products (ethanol, glyoxal, glycolaldehyde, ethylene glycol, acetaldehyde,

Fig. 7. Reactive trajectories for *CO–CHO formation at the high coverage of surface H (H* in 1 ML) from AIMD simulation at 298 K (*A*) one *CHO and one nonadsorbed CO, (*B*) transition state, and (*C*) *CO-CHO. The solvent water molecules are hidden for viewing convenience. The colors are Cu in orange, C in gray, H in yellow, and O in red. The reaction barrier is 0.71 eV.

ethane, and methanol). These computations fully explain experimental observations, including the competition between electrochemical reactions and surface sites.

At *U* greater than −0.6 V, we found that C$_2$H$_4$ formation dominates over CH$_4$ formation. Two *CO couple to form a C–C bond with an energy barrier of 0.69 eV, much lower than for *CHO formation (0.96 eV). Therefore, C$_2$H$_4$ is the major hydrocarbon product for *U* greater than −0.8 V. Interestingly, we find that C$_2$H$_4$ proceeds purely via ER mechanisms, explaining why experiments observe high currents associated with the C$_2$H$_4$ formation in this regime.

For *U* less than −0.6V and *U* greater than −0.8V, H* displaces CO from the surface sites, because H* has a stronger binding energy than CO. Consequently, the surface coverage of H* increases monotonically for more negative potentials, blocking CO adsorption. This decrease of CO surface coverage slows CO dimerization to shut off C$_2$H$_4$ production as *U* = −0.6 V goes to −0.8 V. Of course other factors, such as HER-induced surface reconstruction, deposition of metal impurities (34), and mass diffusion limitation (35), may also contribute to blocking CO adsorption.

At *U* less than −0.8 V, we found that both CH$_4$ and C$_2$H$_4$ are produced by using nonadsorbed CO. Here, *CHO becomes the common intermediate for both CH$_4$ and C$_2$H$_4$ formation.

Considering this full picture of CORR, we see that *U* greater than −0.6 V is the optimum region to obtain hydrocarbon products selectivity. To increase the reaction rates in this regime, we need to accelerate CO dimerization. Ways to achieve this include the following: increasing the local concentration of CO (for example, by modifying the electrolyte or by conjoining the Cu with another element such as Ag or Au that can produce CO from CO$_2$) (36); and increasing the binding energy of CO, perhaps by alloying or using nanotechnologies (37, 38).

Models and Methods

Here, we simulate the water/Cu(100) interface using 48 explicit water molecules on a 4 × 4 Cu(100) surface slab (three layers) as shown in Fig. S1. Two nanoseconds of reactive molecular dynamics (RMD) simulations was carried out to equilibrate the waters interacting with the interface using the ReaxFF reactive force field for Cu and H$_2$O (39). Starting from this well-equilibrated interface, 10 ps of AIMD simulations were carried out at 298 K. Free-energy barriers for various reaction steps and free-energy differences were obtained by using metadynamics (23, 24, 40, 41) and thermodynamic integration (25) for various reaction steps. The collective variables (CV) for elementary reactions are in Tables S1 and S2 and the calculated free energies are in Tables S3 and S4.

CHEMISTRY

Electronic structure calculations were performed within the DFT framework, as implemented in the Vienna ab initio simulation program (VASP) (42–45), a plane-wave pseudopotential package. The exchange and correlation energies were calculated using the Perdew, Burke, and Ernzerhof (PBE) functional within the generalized gradient approximation (GGA) (46, 47). The PBE-D3 method was used to correct van der Waals interaction of water–water and water–Cu (48). The charges on various species were derived using a Bader analysis (49). To compare with the constant potential of experiments, we used the procedure proposed by Chan and Nørskov to remove any artifacts involving work function changes during the chemical reaction (50). The scheme of work function calculation is in Fig. S2. The obtained work functions of

elementary reactions are in Tables S5 and S6 and the corrected free energies are in Tables S7 and S8.

Supporting Information includes models and simulation details, free-energy results, and constant potential corrections.

1. Hori Y, Kikuchi K, Suzuki S (1985) Production of CO and CH_4 in electrochemical reduction of CO_2 at metal electrodes in aqueous hydrogen carbonate solution. *Chem Lett* 14(11):1695–1698.
2. Hori Y, Murata A, Takahashi R (1989) Formation of hydrocarbons in the electrochemical reduction of carbon dioxide at a copper electrode in aqueous solution. *J Chem Soc Faraday Trans* 85(8):2309–2326.
3. Kuhl KP, Cave ER, Abram DN, Jaramillo TF (2012) New insights into the electrochemical reduction of carbon dioxide on metallic copper surfaces. *Energy Environ Sci* 5(5):7050–7059.
4. Kortlever R, Shen J, Schouten KJP, Calle-Vallejo F, Koper MTM (2015) Catalysts and reaction pathways for the electrochemical reduction of carbon dioxide. *J Phys Chem Lett* 6(20):4073–4082.
5. Hori Y (2008) Electrochemical CO_2 reduction on metal electrodes. *Modern Aspects of Electrochemistry*, eds Vayenas C, White R, Gamboa-Aldeco M (Springer, New York), Vol 42, pp 89–189.
6. Gattrell M, Gupta N, Co A (2006) A review of the aqueous electrochemical reduction of CO_2 to hydrocarbons at copper. *J Electroanal Chem* 594(1):1–19.
7. Hori Y, Murata A, Takahashi R, Suzuki S (1987) Electroreduction of carbon monoxide to methane and ethylene at a copper electrode in aqueous solutions at ambient temperature and pressure. *J Am Chem Soc* 109(16):5022–5023.
8. Hori Y, Takahashi R, Yoshinami Y, Murata A (1997) Electrochemical reduction of CO at a copper electrode. *J Phys Chem B* 101(36):7075–7081.
9. Schouten KJP, Kwon Y, van der Ham CJM, Qin Z, Koper MTM (2011) A new mechanism for the selectivity to C1 and C2 species in the electrochemical reduction of carbon dioxide on copper electrodes. *Chem Sci (Camb)* 2(10):1902–1909.
10. Schouten KJP, Qin Z, Pérez Gallent E, Koper MTM (2012) Two pathways for the formation of ethylene in CO reduction on single-crystal copper electrodes. *J Am Chem Soc* 134(24):9864–9867.
11. Schouten KJP, Pérez Gallent E, Koper MTM (2014) The influence of pH on the reduction of CO and to hydrocarbons on copper electrodes. *J Electroanal Chem* 716:53–57.
12. Cheng T, Xiao H, Goddard WA, 3rd (2015) Free-energy barriers and reaction mechanisms for the electrochemical reduction of CO on the Cu(100) surface, including multiple layers of explicit solvent at pH 0. *J Phys Chem Lett* 6(23):4767–4773.
13. Peterson AA, Abild-Pedersen F, Studt F, Rossmeisl J, Norskov JK (2010) How copper catalyzes the electroreduction of carbon dioxide into hydrocarbon fuels. *Energy Environ Sci* 3(9):1311–1315.
14. Nie X, Esopi MR, Janik MJ, Asthagiri A (2013) Selectivity of CO_2 reduction on copper electrodes: The role of the kinetics of elementary steps. *Angew Chem Int Ed Engl* 52(9):2459–2462.
15. Calle-Vallejo F, Koper MTM (2013) Theoretical considerations on the electroreduction of CO to C2 species on Cu(100) electrodes. *Angew Chem Int Ed Engl* 52(28):7282–7285.
16. Hori Y, Takahashi I, Koga O, Hoshi N (2003) Electrochemical reduction of carbon dioxide at various series of copper single crystal electrodes. *J Mol Catal Chem* 199(1-2):39–47.
17. Kim Y-G, Javier A, Baricuatro JH, Soriaga MP (2016) Regulating the product distribution of CO reduction by the atomic-level structural modification of the Cu electrode surface. *Electrocatalysis* 7(5):391–399.
18. Kim Y-G, Baricuatro JH, Javier A, Gregoire JM, Soriaga MP (2014) The evolution of the polycrystalline copper surface, first to Cu(111) and then to Cu(100), at a fixed CO_2RR potential: A study by operando EC-STM. *Langmuir* 30(50):15053–15056.
19. Schouten KJP, Calle-Vallejo F, Koper MTM (2014) A step closer to the electrochemical production of liquid fuels. *Angew Chem Int Ed Engl* 53(41):10858–10860.
20. Montoya JH, Shi C, Chan K, Nørskov JK (2015) Theoretical insights into a CO dimerization mechanism in CO_2 electroreduction. *J Phys Chem Lett* 6(11):2032–2037.
21. Goodpaster JD, Bell AT, Head-Gordon M (2016) Identification of possible pathways for C–C bond formation during electrochemical reduction of CO_2: New theoretical insights from an improved electrochemical model. *J Phys Chem Lett* 7(8):1471–1477.
22. Luo W, Nie X, Janik MJ, Asthagiri A (2016) Facet dependence of CO_2 reduction paths on Cu electrodes. *ACS Catal* 6(1):219–229.
23. Laio A, Parrinello M (2002) Escaping free-energy minima. *Proc Natl Acad Sci USA* 99(20):12562–12566.
24. Iannuzzi M, Laio A, Parrinello M (2003) Efficient exploration of reactive potential energy surfaces using Car-Parrinello molecular dynamics. *Phys Rev Lett* 90(23):238302.
25. Fleurat-Lessard P, Ziegler T (2005) Tracing the minimum-energy path on the free-energy surface. *J Chem Phys* 123(8):084101.
26. Zhang Y-J, Sethuraman V, Michalsky R, Peterson AA (2014) Competition between CO_2 reduction and H_2 evolution on transition-metal electrocatalysts. *ACS Catal* 4(10):3742–3748.
27. Letchworth-Weaver K, Arias TA (2012) Joint density functional theory of the electrode-electrolyte interface: Application to fixed electrode potentials, interfacial capacitances, and potentials of zero charge. *Phys Rev B* 86(7):075140.
28. Petrosyan SA, Rigos AA, Arias TA (2005) Joint density-functional theory: Ab initio study of Cr_2O_3 surface chemistry in solution. *J Phys Chem B* 109(32):15436–15444.
29. Sundararaman R, Goddard WA, 3rd (2015) The charge-asymmetric nonlocally determined local-electric (CANDLE) solvation model. *J Chem Phys* 142(6):064107.
30. Abd Elhamid MH, Ateya BG, Weil KG, Pickering HW (2000) Calculation of the hydrogen surface coverage and rate constants of the hydrogen evolution reaction from polarization data. *J Electrochem Soc* 147(6):2148–2150.
31. Jerkiewicz G (2010) Electrochemical hydrogen adsorption and absorption. Part 1: Under-potential deposition of hydrogen. *Electrocatalysis* 1(4):179–199.
32. Matsushima H, Taranovskyy A, Haak C, Gründer Y, Magnussen OM (2009) Reconstruction of Cu(100) electrode surfaces during hydrogen evolution. *J Am Chem Soc* 131(30):10362–10363.
33. Heyes J, Dunwell M, Xu B (2016) CO_2 reduction on Cu at low overpotentials with surface-enhanced in situ spectroscopy. *J Phys Chem C* 120(31):17334–17341.
34. Hori Y, et al. (2005) "Deactivation of copper electrode" in electrochemical reduction of CO_2. *Electrochim Acta* 50(27):5354–5369.
35. Mistry H, et al. (2016) Highly selective plasma-activated copper catalysts for carbon dioxide reduction to ethylene. *Nat Commun* 7:12123.
36. Rosen J, et al. (2015) Mechanistic insights into the electrochemical reduction of CO_2 to CO on nanostructured Ag surfaces. *ACS Catal* 5(7):4293–4299.
37. Li CW, Ciston J, Kanan MW (2014) Electroreduction of carbon monoxide to liquid fuel on oxide-derived nanocrystalline copper. *Nature* 508(7497):504–507.
38. Manthiram K, Beberwyck BJ, Alivisatos AP (2014) Enhanced electrochemical methanation of carbon dioxide with a dispersible nanoscale copper catalyst. *J Am Chem Soc* 136(38):13319–13325.
39. van Duin ACT, et al. (2010) Development and validation of a ReaxFF reactive force field for Cu cation/water interactions and copper metal/metal oxide/metal hydroxide condensed phases. *J Phys Chem A* 114(35):9507–9514.
40. Ensing B, Laio A, Parrinello M, Klein ML (2005) A recipe for the computation of the free energy barrier and the lowest free energy path of concerted reactions. *J Phys Chem B* 109(14):6676–6687.
41. Laio A, Rodriguez-Fortea A, Gervasio FL, Ceccarelli M, Parrinello M (2005) Assessing the accuracy of metadynamics. *J Phys Chem B* 109(14):6714–6721.
42. Kresse G, Hafner J (1993) Ab initio molecular dynamics for liquid metals. *Phys Rev B Condens Matter* 47(1):558–561.
43. Kresse G, Hafner J (1994) Ab initio molecular-dynamics simulation of the liquid-metal-amorphous-semiconductor transition in germanium. *Phys Rev B Condens Matter* 49(20):14251–14269.
44. Kresse G, Furthmüller J (1996) Efficiency of ab-initio total energy calculations for metals and semiconductors using a plane-wave basis set. *Comput Mater Sci* 6(1):15–50.
45. Kresse G, Furthmüller J (1996) Efficient iterative schemes for ab initio total-energy calculations using a plane-wave basis set. *Phys Rev B Condens Matter* 54(16):11169–11186.
46. Perdew JP, et al. (1992) Atoms, molecules, solids, and surfaces: Applications of the generalized gradient approximation for exchange and correlation. *Phys Rev B Condens Matter* 46(11):6671–6687.
47. Perdew JP, et al. (1993) Erratum: Atoms, molecules, solids, and surfaces: Applications of the generalized gradient approximation for exchange and correlation. *Phys Rev B Condens Matter* 48(7):4978.
48. Grimme S, Antony J, Ehrlich S, Krieg H (2010) A consistent and accurate ab initio parametrization of density functional dispersion correction (DFT-D) for the 94 elements H-Pu. *J Chem Phys* 132(15):154104.
49. Henkelman G, Arnaldsson A, Jónsson H (2006) A fast and robust algorithm for Bader decomposition of charge density. *Comput Mater Sci* 36(3):354–360.
50. Chan K, Nørskov JK (2015) Electrochemical barriers made simple. *J Phys Chem Lett* 6(14):2663–2668.